Chemistry Journals
Analytical, Inorganic, Organic, Physical, Materials Science

Characterization and evaluation of the photocatalytic activity of oxides based on TiO$_2$ synthesized by hydrolysis controlled by the use of water/acetone mixtures

Werick A Machado [Corresp., Equal first author, 1], Antonio Eduardo da Hora Machado [Corresp. Equal first author, 1, 2]

[1] Laboratório de Fotoquímica e Ciência de Materiais, Instituto de Química, Universidade Federal de Uberlândia, Uberlândia, Minas Gerais, Brazil

[2] Unidade Acadêmica Especial de Física, Universidade Federal de Catalão, Catalão, Goiás, Brasil

Corresponding Authors: Werick A Machado, Antonio Eduardo da Hora Machado
Email address: werickalvez@hotmail.com, aeduardo@ufu.br

New photocatalysts based on TiO$_2$ were synthesized and characterized. The synthesis involved the controlled hydrolysis of titanium tetraisopropoxide using water containing different proportions of acetone. X-ray diffraction analyses combined with Raman spectroscopy revealed crystalline oxides characterized by the coexistence of the anatase and brookite phases. The Rietveld refinement of diffractograms showed that the presence of acetone in the synthesis process influenced the composition of these crystalline phases, with the proportion of brookite growing from 13 to 22% with the addition of this solvent in the synthesis process. The BET isotherms revealed that these materials are mesoporous with surface area approximately 12% higher than that of the oxide prepared from hydrolysis using pure water. The photocatalytic potential of these oxides was evaluated by means degradation tests using the dyes Ponceau 4R and Reactive Red 120 as oxidizable substrates. The values achieved using the most efficient photocatalyst among the synthesized oxides were, respectively, 83% and 79% for mineralization, and 100% for discoloration of these dyes. This same oxide loaded with 0.5% of platinum and suspended in a 5:1 v/v water/methanol mixture, produced 56 mmol of gaseous hydrogen in five hours of reaction, a specific hydrogen production rate of 138.5 mmol h^{-1}g^{-1}, a value 60% higher than that achieved using TiO$_2$ P25 under similar conditions.

Characterization and evaluation of the photocatalytic activity of oxides based on TiO$_2$ synthesized by hydrolysis controlled by the use of water/acetone mixtures

Werick Alves Machado[1], Antonio Eduardo da Hora Machado[1,2]

[1] Laboratório de Fotoquímica e Ciência de Materiais, Instituto de Química, Universidade Federal de Uberlândia, Uberlândia, Minas Gerais, Brazil

[2] Unidade Acadêmica Especial de Física, Universidade Federal de Catalão, Catalão, Goiás, Brazil

Corresponding Authors:
Antonio Eduardo da Hora Machado and Werick Alves Machado
Av. João Naves de Ávila, 2121 - Bloco 5K, CEP 38408-100, Uberlândia, MG, Brazil
Email addresses: aehmachado@gmail.com and werickalvez@hotmail.com

Abstract

New photocatalysts based on TiO$_2$ were synthesized and characterized. The synthesis involved the controlled hydrolysis of titanium tetraisopropoxide using water containing different proportions of acetone. X-ray diffraction analyses combined with Raman spectroscopy revealed crystalline oxides characterized by the coexistence of the anatase and brookite phases. The Rietveld refinement of diffractograms showed that the presence of acetone in the synthesis process influenced the composition of these crystalline phases, with the proportion of brookite growing from 13 to 22% with the addition of this solvent in the synthesis process. The BET isotherms revealed that these materials are mesoporous with surface area approximately 12% higher than that of the oxide prepared from hydrolysis using pure water. The photocatalytic potential of these oxides was evaluated by means degradation tests using the dyes Ponceau 4R and Reactive Red 120 as oxidizable substrates. The values achieved using the most efficient photocatalyst among the synthesized oxides were, respectively, 83% and 79% for mineralization, and 100% for discoloration of these dyes. This same oxide loaded with 0.5% of platinum and suspended in a 5:1 v/v water/methanol mixture, produced 56 mmol of gaseous hydrogen in five hours of reaction, a specific hydrogen production rate of 138.5 mmol h^{-1} g^{-1}, a value 60% higher than that achieved using TiO$_2$ P25 under similar conditions.

Introduction

38   Energy and environment are essential and challenging themes for humanity. The growing
39   demand for energy combined with environmental contamination, particularly water
40   contamination, has driven the search for sustainable resources and alternative processes aimed at
41   minimizing negative impacts related to these issues (Cunha et al., 2018; Tractz et al., 2019).
42   Heterogeneous photocatalysis has proving to be a good alternative. Studies have shown
43   its effectiveness in environmental remediation of contaminated waters (Machado et al., 2008;
44   França et al., 2016; Hurtado, Sader & Delgado, 2019), as well as in hydrogen production (H_2), an
45   important energy vector (Bahnemann & Schneider, 2013; Rusinque, Escobedo & Lasa, 2020;
46   Galvão et al., 2019).
47   Much of the efforts spent on expanding the use of heterogeneous photocatalysis were
48   based on the development of new semiconductor materials with increased photocatalytic activity.
49   Among the possible photocatalysts, TiO_2 stands out due to its abundance, insolubility in water,
50   low toxicity, good chemical stability in a wide pH range, and photostability (Kandiel et al.,
51   2010). Despite these desirable characteristics, TiO_2 may present low surface area (depending on
52   the size and shape of crystallites), fast recombination rate of the photogenerated charge carriers
53   (electron/hole) and absorption of radiation in ultraviolet (Bahadori et al., 2020). However, such
54   limitations may be circumvented through structural modifications or by the introduction of
55   dopants (Machado, Alves & Machado, 2019; Santos et al., 2015a; Martin-Somer et al., 2020).
56   TiO_2 presents itself according to three distinct crystalline phases: brookite, with
57   orthorombic structure, anatase and rutile, both with tetragonal structure, widely used in
58   heterogeneous photocatalysis (Fujishima, Zhang & Tryk, 2008). Experimental and theoretical
59   studies suggest that a high percentage of anatase phase and small fraction of brookite guarantees
60   greater photocatalytic activity to TiO_2, compared to pure anatase, due the existence of structural
61   defects that end up delaying the displacement of electrons and holes, minimizing the
62   recombination between load carriers, making more reactive the surface of the photocatalyst
63   (Jiang et al., 2014; Di Paola, Berllardita & Palmisano, 2013).
64   Efforts have been spent on improving methods that allow the control and reproducibility
65   of the synthesis of this kind of material, which allows the obtaining of particles with mixed
66   crystalline phase, with high photocatalytic yield (Luevano-Hipolito et al., 2014; Mohammadi,
67   Harvery & Boodhoo, 2014; Myilsamy, Murugesan & Mahalakshmi, 2015). In this sense, an
68   approach that has proved feasible is the use of solvent combinations in the manipulation of the
69   material mesostructure. Kumar and collaborators showed that sol-gel synthesis in a system
70   involving the combination of different solvents strongly interferes with precursor hydrolysis,
71   improving the structural properties of oxides (Kumar et al., 1999).
72   In the present study, we performed the modified sol-gel synthesis of TiO_2-based
73   photocatalysts aiming to improve their photocatalytic activities. The precursor (titanium
74   tetraisopropoxide) hydrolysis rate was controlled by the use of different proportions of acetone
75   as co-solvent, reducing the availability of water in the process. With this, greater control of the
76   formation and growth of critical nuclei was possible, avoiding the formation of very crowded
77   particles. The synthesized oxides were characterized by X-ray diffraction (XRD), Raman

78 spectroscopy, diffuse reflectance, specific surface area measurements (BET) and transmission
79 electron microscopy (TEM). The photocatalytic activity of these compounds was evaluated in
80 promoting the photodegradation of two azo dyes, used as oxidizable substrates: Ponceau 4R
81 (P4R) and Reactive Red 120 (RR120). The best and least efficient photocatalyst, along with the
82 TiO2 P25, were confronted in terms of hydrogen production capacity. The reuse potential of the
83 best photocatalyst was also evaluated.
84

Materials & Methods

Experimental

87   All reagents used (titanium tetraisopropoxide, 97%; isopropanol, 99.5%; ponceau 4R
88 (P4R), 75%; reactive red 120 (RR120) - purity not informed by the supplier; Methanol, 99.8%;
89 hexahydrated hexachloroplatinic acid, 37.5%; hydrochloric acid, 37% and sodium hydroxide,
90 98%) were of analytical grade, provided by Sigma-Aldrich. Acetone 99.5%, was provided by
91 Synth. All solutions were prepared with ultrapure water obtained from an Elix 5 Milli-Q® water
92 purification system.

Preparation of photocatalysts

94   The oxides were obtained by the sol-gel method, involving the solubilization of titanium
95 tetraisopropoxide in isopropanol at 3°C under ultrasonic stirring for 20 minutes, followed by its
96 hydrolysis by the addition of water/acetone mixture by drip and precipitation under ultrasonic
97 stirring.
98   The water/acetone mixtures were prepared with deionized water and different proportions
99 of acetone (0%, 25%, 50% and 75% v/v). The resulting amorphous solids were washed with
100 distilled water, centrifuged and sintered using a conventional oven at 400 ºC for 5 hours.
101   The standard photocatalyst, synthesized in aqueous medium, was called W1. The other
102 oxides, synthesized by hydrolysis using different water/acetone mixtures (25%, 50%, 75% v/v of
103 acetone), were named W1-25, W1-50, W1-75, respectively.

Characterization of the photocatalysts

105   The photocatalysts were characterized by different methodologies. By X-ray diffraction
106 (XRD) using a XDR600 (Shimadzu) powder diffractometer operating at 40 kV and 120 mA,
107 using Cu Kα radiation. The diffractograms were scanned in the range between 10 and 80º under
108 a rate of 0.5º min^{-1}. Finally, they were refined by the method of Rietveld using the software
109 "*FullProf*" (Roisnel & Rodriguez-Carvajal, 2011). As criteria of mounting, the S factors were
110 maintained between 1.22 and 1.31 (**Table S1**, Supplementary Information).
111   The Raman spectra were acquired at room temperature using a Bruker RFS 100/S
112 spectrometer coupled to a 1064 nm laser operating at 100 mW. Each Raman spectrum, with
113 spectral resolution of 4 cm^{-1}, is the result of the accumulation of 128 scans.

114   The diffuse reflectance spectra were obtained using a double beam UV-1650 (Shimadzu)
115 spectrophotometer, estimating the band energy by Kubelka-Munk treatment (Patterson, Shelden
116 & Stockton, 1997). In these measures, barium sulfate was used as reference.
117   The N_2 adsorption-dessorption isotherms were obtained using an ASAP 2020
118 (Micrometrics) analyser. The adsorption data were analysed by the method proposed by
119 Brunauer, Emmett and Teller (BET) for the surface area and the method of Barrett-Joyner-
120 Halenda (BJH) for pore volume.
121   Transmission electron microscopy (TEM) images were obtained using a JEM-2100 (Jeol)
122 microscope. In the preparation of the samples, suspensions containing the powders dispersed in
123 acetone were used with the aid of a cutting-edge ultrasound. These suspensions were deposited
124 on copper grids and air dried. From the images, obtained with the aid of the image editing
125 software "*ImageJ*", it was possible to calculate the particle size randomly selecting
126 approximately 100 particles per image.

127 *Photocatalytic assays*

128   4 L of an aqueous solution containing 100 mg L^{-1} of the photocatalyst were used in the
129 photodegradation assay, in combination with a concentration equivalent to 12.0 ppm of dissolved
130 organic carbon of the dye - corresponding to 31.3 mg L^{-1} of P4R or 43.5 mg L^{-1} of RR120 – used
131 as oxidizable substrates. Detailed experimental assembly for the photodegradation assays was
132 described in a previous study (Oliveira et al., 2012).
133   A commercial high-pressure mercury lamp (HPLN) of 400 W (Philips, 2015) without the
134 protective bulb was employed as radiation source. Under this condition, its estimated photonic
135 flux in the UVA was of 3.3 x 10^{-6} Einstein/s (Machado et al., 2008), with an irradiance inside the
136 reactor of 100 W / m^2. During discoloration and dye mineralization monitoring, aliquots were
137 collected every 20 minutes, in a total reaction interval of 140 minutes. The dyes discoloration
138 was monitored by varying the absorbance of the solutions with the reaction time, without pH
139 correction. Monitoring was done in the maximum absorbance wavelength in the visible of each
140 dye - 507 nm for P4R and 512 nm for RR120 - using a UV-1201 (Shimadzu) spectrophotometer.
141 Mineralization was monitored from dissolved organic carbon (DOC) measurements, using a
142 TOC-VCPH/CPN (Shimadzu) analyser, aiming to identify the most efficient photocatalyst. For
143 this, the experiments were restricted to the monitoring of P4R photodegradation. The most
144 efficient photocatalyst was also submitted to photodegradation tests using Remazol Red
145 (RR120), comparing its performance with that presented by the commercial catalyst Evonik
146 Degussa TiO_2.
147   These assays were conducted at least in triplicate and separately for each dye.
148   The reuse of the most efficient photocatalyst was evaluated using P4R as oxidizable
149 substrate. For this, after each reaction the photocatalyst was separated from the supernatant by
150 decanting, washed with distilled water, centrifuged and dried at 70°C for 24 hours, and then
151 reused under the same described conditions using a new load of the same dye. Each test was
152 performed in quadruplicate in order to compensate for the losses that occurred during the
153 washing of the catalyst, in order to ensure a constant mass of this in each cycle.

154   Subsequently, hydrogen production assays were done using the most effective
155   synthesized photocatalyst, as well as the commercial catalyst Evonik Degussa TiO_2 and the W1
156   oxide. In these experiments, the concentration of catalyst was similar to that used in the assays of
157   dye degradation, being this oxide loaded by photoreduction with 0.5% m/m of Pt, furnished by a
158   solution of hexachloroplatinic acid. So, the Pt-loaded photocatalyst was then suspended in 750
159   ml of a water/methanol mixture containing 20% v/v of methanol, this last being used as
160   sacrificial reagent. These assays occurred under continuous stirring. The pH of the reaction
161   medium was adjusted in 6.2 using solutions 0.1 mol L^{-1} of HCl or NaOH. Finally, the potential
162   of reuse of the photocatalyst used in such assays was evaluated in at least three photocatalytic
163   cycles. In the reuse assays, only the pH adjustment of the reaction medium was performed at the
164   beginning of each new cycle. The first cycle was equivalent to the first hydrogen production test,
165   carried out for five hours. Thus, the total reaction time was 15 hours.
166   For all photocatalytic assays the results are the averages of at least three individual
167   experiments.
168   For operator protection and better use of radiation produced by the lamp, the reactor was
169   positioned in a box internally covered with aluminum film, **Fig 1**.
170
171   Figure 1 – Image of the assembly used in hydrogen production assays: a) external view, b)
172   internal view.
173
174   The reactor, built in borosilicate glass, has a cooling jacket connected to a thermostat bath on
175   its outside which keeps the temperature of the reaction medium stabilized at 20ºC throughout the
176   reaction. Before each experiment, the reactor was purged with N_2 for 20 minutes to eliminate
177   dissolved gases, especially oxygen. The same HPLN lamp reported above was used as radiation
178   source. For analysis of the gases produced during the reaction, aliquots of 1 mL of these gases
179   were collected at intervals of 30 minutes of reaction, in a total period of 5 hours. These samples
180   were analyzed at 230°C in a Shimadzu GC-17A gas-phase chromatograph equipped with thermal
181   conductivity detector (TCD) and a *Carboxen™ 1010 Plot* capillary column. Argon, with flow of
182   40 ml min^{-1}, was employed as carrier gas.
183

184   **Results and Discussion**
185   *Characterizations*

186   By analyzing the X-ray diffraction (XRD) data, **Fig 2**, it is possible to infer that all oxides
187   have well-defined diffraction peaks suggesting crystallinity for these materials most likely due to
188   the heat treatment used in the synthesis process. In addition, according to reports found in the
189   literature and the crystallographic files JCPDS 21-1272 (anatase) and 29-1360 (brookite), all
190   oxides exhibit major peaks characteristic of the anatase phase, and secondary peaks related to the
191   brookite phase (Di Paola, Bellardita & Palmisano, 2013; Neto et al., 2017; Patrocinio et al.,
192   2015; Hu, Tsai & Huang, 2003).

193

194   Figure 2 - X-Ray diffratogram of the studied oxides.

195

196   The mean size and mean deformation of crystallite were calculated from the data

197   obtained from the Rietveld refinement, as presented in **Table 1**. The diffractograms,

198   accompanied by the respective calculated diffraction profiles, experimentally obtained profiles,

199   and residual curves and Bragg diffractions adjusted by Rietveld method can be seen in

200   **Supplementary Figure 1**, in the Supplementary Information.

201

202   Table 1 - Percentage of crystalline phase, crystallite size and medium deformation, obtained by

203   Rietveld refinement for synthesized oxides.

204

205   Rietveld refinement data demonstrates that the percentage of brookite phase increases

206   from 13% to 22% with the addition of acetone as co-solvent in the hydrolysis of titanium

207   tetraisopropoxide. Despite this, the increase in the proportion of acetone from 25% to 75% did

208   not result in an equivalent increase in the percentage of brookite phase, suggesting that the use of

209   acetone only interfered in hydrolysis, affecting the organization of critical nuclei in the

210   oligomeric network of titanium, in order to preorder the crystallization of the mentioned phase.

211   On the other hand, the average crystallite size of the anatase phase was about 30% lower for W1-

212   75, compared to the other oxides, including the W1, where there was no addition of acetone

213   during its synthesis. This suggests that the excess of acetone should promote a significant

214   reduction in the average crystallite size of the anatase phase, favoring the increase in the average

215   crystallite size of brookite. Thus, the mean deformation of the crystallite follows the same trend,

216   i.e., if the secondary phase becomes larger it will present larger deformations, when compared

217   with the primary phase.

218   As in the X-ray diffractograms, the Raman spectra also evidence the mixed composition

219   of two crystalline phases, **Fig 3**. In all oxides, five main bands attributed to the anatase phase are

220   observed respectively at 145 cm^{-1} (E$_g$), 198 cm^{-1} (E$_g$), 399 cm^{-1} (B$_{1g}$), 519 cm^{-1} (B$_{1g}$) and 640 cm^{-}

221   ^{1} (E$_g$) (Sahoo et al., 2009). Between 200 and 500 cm^{-1} four bands of lower intensity are observed:

222   at 247 cm^{-1} (A$_{1g}$), 323 cm^{-1} (B$_{1g}$), 368 cm^{-1} (B$_{2g}$) and 456 cm^{-1} (B$_{2g}$), attributed to the phase

223   brookite. In addition to these bands, this phase features a band of greater intensity around 150

224   cm^{-1} which may be superimposed with the band identified at 145 cm^{-1}, attributed to anatase, thus

225   influencing the width of the E$_g$ Raman mode (Di Paola, Bellardita & Palmisano, 2013; Iliev,

226   Hadjiev & Litvinchuk, 2013).

227

228   Figure 3 - Raman spectra of the synthesized photocatalysts. Insert: peaks at 247 cm^{-1}, 323 cm^{-1},

229   368 cm^{-1}, 456 cm^{-1} attributed to brookite.

230

231   From the expanded spectrum, **Fig 4**, it was possible to observe a small enlargement of the

232   band centered at 145 cm^{-1} in the Raman spectrum of the photocatalyst W1-75. This effect should

233 be related to the smaller particle size since the lifetime of the vibrational mode tends to be
234 shorter as particle size decreases, which ends up resulting in band enlargement (Liu et al., 2012;
235 Zhu et al., 2012).

236

237 Figure 4 - Expanded Raman spectra in the region between 120 and 180 cm^{-1} for the synthesized
238 photocatalysts.

239

240   From the diffuse reflectance spectra, **Fig 5 - Insert**, expressed in terms of the Kubelka-
241 Munk's function, **Fig 5**, and by applying the direct method, it was possible to estimate the *band*
242 *gap* energies (Eg) of the photocatalysts (Liu & Li., 2012). The estimated Eg were as follows:
243 3.23 eV for W1, 3.24 eV for W1-25, 3.22 eV for W1-50, and 3.23 eV for W1-75, indicating that
244 the estimated *band gap* energies have not undergone major changes, which agree with the data
245 reported in the literature for pure TiO_2 (Martin-Somer et al., 2002; Neto et al., 2017; Resende et
246 al., 2017). Most likely, this stems from the synthesis conditions adopted in this work, where none
247 dopant material was added. It is known that the E_g displacement to lower energies occurs
248 preferably in synthesis that promote the doping of oxides with metal cations (Santos et al.,
249 2015a), non-metallic anions (Liu et al., 2014), co-doping (Kuvarega, Krause & Momba, 2015),
250 and self-doping (Chen et al., 2011).

251

252 Figure 5 - Diffuse reflectance spectra expressed in terms of Kubelka-Munk's function. Insert: %
253 Reflectance vs. wavelength (nm) spectra for the synthesized photocatalysts.

254

255   As for N_2 adsorption and desorption of these oxides, **Fig 6**, the analysis of the adsorption-
256 desorption isotherms suggests that they are type IV (IUPAC., 1985), characteristic of
257 mesoporous materials with an average pore diameter between 2 and 50 nm, **Table 2**. Hysteresis
258 profiles are very close to those of type H2, associated with more complex mesoporous structures,
259 in which the distribution of pore sizes and their shape are not well defined (Guan-Sajonz et al.,
260 1997). It is also evident that the photocatalysts W1-50 and W1-75, synthesized by hydrolysis
261 using the highest percentages of acetone, present slightly more steeper isotherms compared to the
262 oxides W1 and W1-25, also exhibiting greater heterogeneity in pore distribution compared to
263 these same oxides.

264

265 Figure 6 – N_2 adsorption-desorption isotherms obtained for the studied photocatalysts.

266

267 Table 2 - Morphological parameters related to synthesized photocatalysts.

268

269   **Table 2** presents the morphological parameters related to the synthesized oxides. In
270 general, oxides obtained from hydrolysis using water/acetone mixtures did not undergo
271 significant morphological changes, since for W1 the oxide porosity is practically the same
272 presented by W1-50 and W1-75. On the other hand, the surface area of these two oxides is

273 between 10 and 12% larger than that of W1. This may favor the adsorption of organic matter on
274 their surfaces, which can consequently favor the photocatalytic efficiency. In addition, it was
275 observed an inverse correlation between the surface area and the average particle size, except for
276 the W1-25 that presented wide variation on its particle size.
277
278   The TEM images, **Fig 7**, suggest a dense aspect to the particles, which have irregular
279 spherical shape and a strong tendency to aggregation, giving rise to clusters of TiO_2. This should
280 be related to the high level of hydrolysis provided by the synthesis method (Jiang, Herricks &
281 Xia, 2003). However, agglomeration appears to have been minimized by the addition of acetone
282 as co-solvent in hydrolysis, evidencing that its use decreased the hydrolysis rate of the precursor.
283 This, consequently, should favor particle dispersion. On the other hand, the particle sizes
284 estimated from these images do not suggest a role of acetone on this property, as can be seen by
285 the values estimated for the particle size: (14 ± 1) nm, (17 ± 3) nm, (10 ± 1) nm and (13 ± 1) nm,
286 respectively for W1, W1-25, W1-50 and W1-75. The histograms can be viewed in
287 **Supplementary Figure 2**, in the Supplementary Information.
288
289 Figure 7 – Images obtained by TEM for synthesized oxides a) W1, b) W1-25, c) W1-50, d) W1-
290 75.
291

292 ***Photocatalytic activity: Degradation/mineralization of organic compounds***

293   The **Table 3** presents the photocatalytic performance of the synthesized oxides and of the
294 commercial oxide TiO_2-P25, in the degradation of the two azo dyes used as oxidizable substrates
295 in this study. For comparative purposes, the dyes were also submitted to direct photolysis, in order
296 to evidence the role of the photocatalysts in the photodegradation.

297

298 Table 3 - Photocatalytic performance of synthesized oxides and TiO2-P25 compared with direct
299 photolysis, in the degradation of the dyes Ponceau 4R (P4R) and Remazol Red 120 (RR120).

300

301   The discoloration (k_{dis}) and mineralization (k_{min}) rate constants were estimated from the
302 application of the kinetic model of Languimir-Hinschelwood (Hoffmann et al., 1995; Machado et
303 al., 2012), considering that the kinetic regimen in these photocatalytic processes follows a
304 pseudo-first order kinetics (Machado et al., 2003; Machado et al 2012; Santos et al., 2015a;
305 França et al., 2016). Graphs containing the kinetic data corresponding to these values are
306 presented in the Suplementary Information **(Supplementary Figures 3**, **4** and **5)**.
307   The expected low efficiency both in degradation and discoloration via direct photolysis,
308 compared to the results achieved by the photocatalysts can be related to the energy of the
309 incident photons, provided by the radiation source (Machado et al., 2008), and to the very low

310 rate of formation of radical species, produced by homolytic scission of labile bonds present in
311 these dyes (Kumar et al., 1999).
312   In the experiments involving the participation of the photocatalysts, the degradation
313 occurred more efficiently due the participation of reactive oxygen species, among them the
314 hydroxyl radicals (HO·) and superoxide radical-ions ($O_2^{·-}$), generated mainly by water
315 decomposition. Such species, due their low selectivity (Machado et al., 2012), together with
316 secondary radical species produced during the photocatalytic process, tend to promote the
317 oxidation of organic substrates present in the reactional medium (Oancea & Meltzer, 2014;
318 Santos at al 2015b). The dissolved oxygen, present in the aqueous medium, as example, when
319 reduced by the semiconductor, contributes with the formation of $O_2^{·-}$ and perhydroxyl radicals,
320 which, although less oxidizing than HO· (Machado et al., 2012), are very important in promoting
321 the degradation of organic substrates.
322   The values of the apparent rates of discoloration and mineralization, observed in the
323 reactions mediated by the photocatalysts evaluated in the present study, **Supplementary Figure**
324 **3** – Supplementary Information, suggest that these reactions occur in two stages, following
325 kinetics of apparent pseudo-first order. Initially, the reaction occurs at a rate lower than in the
326 second stage, when the apparent rate constant, in some cases, is three times higher. The higher
327 rate constant in the second stage should be a consequence of the more favored adsorption of the
328 fragments of organic matter formed in the first stage of the process, combined with the good
329 availability of oxygen and water, important for the formation of radicals responsible for the
330 oxidation of organic matter (França et al., 2016).
331   The mineralization of P4R mediated by the oxides W1-25, W1-50 and W1-75 increased
332 respectively 5.7%, 18.6% and 24.3% more than the result obtained using W1, when 70%
333 mineralization was achieved. It is noteworthy that the hydrolysis process which gave rise to this
334 oxide, occurred exclusively in the presence of water. It should be noted that the mineralization
335 achieved using TiO_2 P25 as photocatalyst was only 8% higher than that obtained when W1-75
336 was employed.
337   Although the mineralization and discoloration of P4R conducted using W1-75 presented
338 the best performance among the synthesized oxides, the result observed was only 4.8% higher
339 than that achieved using W1-50. Considering the proportion of acetone used in the synthesis of
340 W1-75 and its limited photocatalytic performance, W1-50 was then considered as the most
341 effective catalyst for mineralizing P4R, being therefore preferably applied in the following stages
342 of the present study. Since W1-25 presented intermediate performance to that observed for the
343 W1 and W1-50 catalysts, evaluating its efficiency, regarding the degradation of RR120, was
344 therefore considered unnecessary.
345   The good photocatalytic activity presented by these oxides, in particular the W1-50, can
346 be attributed mainly to the mixed composition of the phases and high crystallinity obtained after
347 heat treatment, confirmed by the XRD and Raman spectra. The presence of an additional phase
348 tends to introduce defects that tend to favor the photocatalytic activity of a photocatalyst
349 (Kandiel et al., 2010). Brookite, for having conduction band approximately 0.14 eV more

350 negative than anatase, ends up favoring the interfacial electron transfer by imposing an energy
351 barrier for the return of the excited electrons to the valence band of anatase, which tends to favor
352 the coexistence of charge carriers (Kandiel et al., 2010; Di Paola, Bellardita & Palmisano, 2013;
353 Patrocinio et al., 2015).
354   Reuse assays were performed using the recycled W1-50 in the photocatalytic degradation
355 of the dye P4R. The recycled W1-50 was separated by decantation after the first photocatalytic
356 test. It was then washed with distilled water, centrifuged and dried at 70°C for 24 hours. After
357 this procedure, the recycled oxide was used to promote the degradation of P4R present in a new
358 solution. The discoloration level remained at 100% while the mineralization performance
359 decreased about 30%. This loss of performance should be related to photocatalyst poisoning
360 caused by species adsorbed on the catalyst at the end of each photocatalytic cycle, compromising
361 the availability of active sites (Nakhjavani et al., 2015). It is important to consider that the
362 recycled catalyst was not submitted to any prior purification procedure aiming the removal of
363 contaminants incorporated by adsorption the previous cycles. The discoloration and
364 mineralization profiles, as well as the kinetics of discoloration and mineralization in this reuse
365 assay, are available in the Supplementary Information, **Supplementary Figure 4**.
366   **Table 3** also presents the performance of the oxides W1, W1-50 and TiO_2 P25 in the
367 mineralization and discoloration of the dye RR120. In this case, although RR120 has a more
368 complex chemical structure than P4R, presenting two azo groups and two triazine groups, the
369 performance achieved by W1-50 was comparable to that presented when using TiO_2 P25
370 differing only by the kinetic constants of mineralization (k_{min}). The residual total organic carbon
371 (TOC) observed after degradation of both P4R and RR120 (**Supplementary Figures 3** and **5,**
372 Supplementary Information), should be related to the presence of short-chain carboxylic acids,
373 recalcitrant to photocatalytic degradation (França et al., 2016). Studies have shown that the
374 triazine groups present in the chemical structure of RR120, when photocatalytically oxidized,
375 give rise to cyanuric acid, very resistant to degradation (Hu & Wang, 1999; Wang, 2000;
376 Camarillo & Ricon, 2011).

Photocatalytic hydrogen production

378   The profiles of hydrogen production as function of the reaction time, **Fig 8**, show a
379 superior performance of W1 and W1-50 compared to TiO_2-P25.
380
381 Figure 8 – Photocatalytic hydrogen production vs reaction time.
382
383   The process mediated by W1-50 produced approximately 56 mmols of gaseous H_2, while
384 in the same period TiO_2 P25 produced 43% less. On the other hand, W1 produced approximately
385 3% less hydrogen than W1-50. In addition, it is explicit that the production of H_2 using the
386 oxides presented in this study increased until the end of the assay, suggesting that the
387 photocatalytic process was still in its propagation stage. H_2 production using TiO_2 P25 presented
388 a different profile, suggesting typical accommodation of processes in stages near termination. It

389   is known that TiO_2 P25 is the result of the crystalline composition between anatase and rutile.
390   The advantage of the photocatalysts presented in this work should be in the combination of
391   anatase and brookite that tends to increase the photocatalytic efficiency of the semiconductor.
392   Liu and coworkers (Liu et al., 2014), for example, demonstrated that the recombination of the
393   photoinduced charge carriers is minimized when the semiconductor oxide have a structure based
394   on this kind of phase composition. This behavior occurs due to the most negative cathode
395   potential of the conduction band of the brookite phase, more negative than the proton reduction
396   potential and the cathode potential of the conduction band of anatase, thus favoring its
397   conversion to H_2 (Kandiel et al., 2010; Patrocinio et al., 2015; Tay et al., 2013). Besides, this
398   phenomenon facilitates the interfacial transfer of electrons while an energy barrier is established,
399   which hinders their return, thereby prolonging the coexistence of the charge carriers. With this,
400   both the oxidative (metanol oxidation) and the reductive process (H_2 production) end up being
401   favored.
402   In terms of specific hydrogen production rate (SHPR), the production mediated by W1-50
403   (138.5 mmol h^{-1} g^{-1}) was 60 % higher than the achieved using TiO_2 P25 (86.4 mmol h^{-1} g^{-1}).
404   Even the SHPR of W1 (126.5 mmol h^{-1} g^{-1}) was higher than that of the commercial
405   photocatalyst. It is observed, therefore, that the variant of the sol-gel synthesis proposed in this
406   study resulted in pure photocatalysts, such as the W1-50, which present SHPR much higher than
407   that of TiO_2 P25, as well as of photocatalysts recently reported in the literature. Selcuk and
408   coworkers (Selcuk, Boroglu & Boz, 2012), in a study involving a catalyst resulting from TiO_2
409   codopage with platinum and nitrogen, reported, under the best operating conditions, a TEPH of
410   13 µmol $h^{-1}g^{-1}$, a value significantly lower than the achieved using W1-50. This study involved
411   the use of a 400 W mercury lamp as a source of radiation and a solution containing 10%
412   methanol. In another study, Lin and Shih, (Lin & Shih, 2016) using a TiO_2 doped with copper
413   and nitrogen, obtained a TEPH equal to 27.4 mmol h^{-1} g^{-1}, a value approximately 5 times lower
414   than the achieved using the W1-50 in the present study. These authors also used a 400 W
415   mercury lamp as a source of radiation. In this case, the catalyst was suspended in a solution
416   containing 20% methanol.
417   In addition, the reuse of the W1-50 was evaluated for the collection of information related
418   to its photostability. These tests consisted in evaluating the reproducibility of the catalytic action
419   of this oxide by performing three consecutive photocatalytic cycles of five hours each using the
420   same initial conditions applied to the system, with the exception of the pH of the medium,
421   adjusted at the beginning of each additional cycle. These results are presented in **Fig 9**.
422
423   Figure 9 – Amount of H_2 produced by W1-50 in three photocatalytic cycles.
424
425   Although there is an increase in H_2 production in the other cycles, compared to the first
426   cycle, during the photocatalytic cycles W1-50 presented a similar profile of H_2 production in the
427   three cycles, **Fig 9**. In the second cycle, the SHPR increased by about 10% (154.7 mmol $h^{-1}g^{-1}$)
428   compared to the first cycle, whereas in the third cycle this increase was of 9%. The good

429   photostability, reproducibility and significant yield in H_2 production during these experiments
430   may be related to the absence of contaminants in the catalyst in the different cycles. Certain
431   oxides based on TiO_2, obtained from associations, anchoring and doping with other substances,
432   show losses in the capability of H_2 production as the photocatalytic cycles succeed. The reason
433   for this has been pointed out as being due the photodesorption of compounds associated or
434   anchored or by photoreduction of metals on TiO_2 surface, thus contaminating the reaction sites
435   (Zhang et al., 2013; Yuan et al., 2015).

436
437
438

439   ## Conclusions

440   In the present study, we show the use of acetone as a cosolvent in the hydrolysis of
441   titanium tetraisopropoxide interfered favorably in the organization of critical nuclei in the
442   oligomeric network of Titanium, in order to preorder phase crystallization brookite, thereby
443   expanding the photocatalytic activity of the synthesized oxides. The results obtained by DRX
444   analysis, together with the subsequent Rietveld refinement, demonstrated that the synthesized
445   oxides are crystalline, with the percentage of brookite phase ranging from 13% to 22%, from W1
446   to W1-50. The changes in the surface area is influenced by the presence of acetone during the
447   hydrolysis process, verified by the increase of 12% for W1-50 compared to that of W1. On the
448   other hand, the estimated band gap energies have not undergone significant changes in view of
449   the synthesis conditions.

450   During the photodegradation assays, the W1-50 was defined as the most effective
451   photocatalyst based on P4R degradation, when 83% mineralization and 100% discoloration were
452   achieved. In reuse assays using the same catalyst and new charges of the same dye, it was
453   possible to achieve the same level of discolouration. However, the mineralization was impaired
454   by the lack of previous treatment of the catalyst between the cycles of reuse, reaching only 58%
455   of mineralization. On the other hand, in the degradation of the dye RR120 the performance of
456   W1-50 was comparable to that obtained using TiO_2 P25, with 100% discoloration and 79%
457   mineralization.

458   Regarding the photocatalytic production of hydrogen using W1-50 as a catalyst, 56
459   mmols of gaseous hydrogen were produced in 5 hours of reaction, which corresponds to a
460   specific hydrogen production rate (SHPR) of 138.5 mmol $h^{-1} g^{-1}$, a value 60% higher than that
461   achieved when TiO_2 P25 was employed. In addition, the reuse assays demonstrated the very
462   good photostability and effectiveness of W1-50, which also ensured an increase of 10% in SHPR
463   in the succession of cycles.

464   Thus, the changes introduced in the structure of TiO_2 by the use of water-acetone
465   mixtures during the hydrolysis of titanium tetrahydropropoxide resulted in materials with

466 improved photocatalytic performance both in the degradation/mineralization of organic dyes and
467 in the photocatalytic production of hydrogen. The reason for this good performance may be
468 related to hydrolysis retardation, favoring the obtaining of more ordered and mesoporous oxides,
469 with expressive surface area. It is important to emphasize that the synthesis process favored the
470 increase in the composition of crystalline phases, stimulating the increase in the proportion of
471 brookite, which tends to favor the delay in the recombination of the photoinduced charge carriers
472 (electron/hole), expanding the photocatalytic performance and especially regarding the
473 production of gaseous hydrogen.

474
475

Acknowledgements

477   The authors thank to Professor L. F. Cappa de Oliveira (NEEM-UFJF) for the RAMAN
478 spectrum measures; to CETENE/LMNANO for the BET measures; to Professor C. E. Hori for
479 making the LPS/FEQUI - UFU facilities available for H_2 detection by gas chromatography.
480 W.A.M. is particularly indebted to CAPES Foundation by his Doctoral Scholarship.

481

482

References

485 **Bahadori E, Ramis G, Zanardo D, Menegazzo F, Sigoretto M, Gazzoli D, Pietrogiacomi
486 D, Di Michele A, Rossetti I. 2020**. Photoreforming of Glucose over CuO/TiO₂. *Catalysts*,
487 **10**, 477-498. https://doi.org/10.3390/catal10050477

489 **Bahnemann DW, Schneider J. 2013.** Undesired role of sacrificial reagents in
490 photocatalysis. *J. Phys. Chem. Lett.* **4**, 3479- 3483. https://doi.org/10.1021/jz4018199

492 **Camarillo R, Ricón J. 2011.** Photocatalytic Discoloration of Dyes: Relation between Effect
493 of Operating Parameters and Dye Structure. *Chem. Eng. Technol*. **34**, 1675-1684.
494 https://doi.org/10.1002/ceat.201100063

496 **Chen X B, Liu L, Yu PY, Mao SS. 2011.** Increasing Solar Absorption for Photocatalysis
497 with Black Hydrogenated Titanium Dioxide Nanocrystals. *Science*. **331**, 746-750.
498 https://doi.org/10.1126/science.1200448

500 **Cunha DL, Kuznetsov A, Achete CA, Machado AEH, Marques M. 2018.** Immobilized
501 TiO₂ on glass spheres applied to heterogeneous photocatalysis: photoactivity, leaching and
502 regeneration process. *PeerJ*. 1-19. https://doi.org/10.7717/peerj.4464
503

504 **Di Paola A, Bellardita M, Palmisano L. 2013**. Brookite, the Least Known TiO_2
505 Photocatalyst. *Catalysts*, **3**, 36-73. https://doi.org/10.3390/catal3010036
506

507 **França MD, Santos LM, Silva TA, Borges KA, Silva VM, Patrocinio AOT, Trovó AG,**
508 **Machado AEH. 2016**. Efficient Mineralization of Paracetamol Using the Nanocomposite
509 TiO2/Zn(II) Phthalocyanine as Photocatalyst. *J. Braz. Chem. Soc*. **27**, 1094.
510 http://dx.doi.org/10.5935/0103-5053.20160007
511

512 **Fujishima A, Zhang XT, Tryk DA. 2008**. Modification of the Surface Properties of Core-
513 Shell Semiconductors and Their Effects on the Photodecolorization Activity and Adsorption.
514 *Surf. Sci. Rep*, **63**, 515-582. https://doi.org/10.1016/j.surfrep.2008.10.001
515

516 **Galvão RA, Barreto PBB, Soares TAS, Sales LBV, Santos JM, Santa-Cruz LA, Seeger**
517 **TS, Duarte FA, Silva GM, Machado G. 2019**. Nanostructured Systems Obtention Using
518 LbL Self-Assembly or the Cysteine-Assisted Adsorption Method and Their Application as a
519 Water Splitting Single Catalyst. *J. Braz. Chem. Soc*. **30**, 2599-2609**.**
520 http://dx.doi.org/10.21577/0103-5053.20190176
521

522 **Guan-Sajonz H, Guiochon G, Davis E, Gulakowski K, Smith, DW. 1997.** Study of the
523 physico-chemical properties of some packing materials: III. Pore size and surface area
524 distribution. *J. Chromatogr. A.,* **773**, 33-51. https://doi.org/10.1016/S0021-9673(97)00201-X
525

526 **Hoffmann M, Martin S, Choi W, Bahnemann, DW. 1995.** Environmental Applications of
527 Semiconductor Photocatalysis. *Chem. Ver*. **95**, 69-96. https://doi.org/10.1021/cr00033a004
528

529 **Hu C, Wang Y. 1999.** Decolorization and biodegradability of photocatalytic treated azo dyes
530 and wool textile wastewater. *Chemosphere*. **39**, 2107-2115. https://doi.org/10.1016/S0045-
531 6535(99)00118-6
532

533 **Hu Y, Tsai HL, Huang CL. 2003**. Effect of brookite phase on the anatase–rutile transition
534 in titania nanoparticles. *J. Eur. Ceram. Soc*. **23**, 691-696. https://doi.org/10.1016/S0955-
535 2219(02)00194-2
536

537 **Hurtado SM, Sader KM, Delgado ADG. 2019.** Computer-aided simulation and exergy
538 analysis of TiO_2 nanoparticles production via green chemistry. *PeerJ*. 1-19.
539 https://doi.org/10.7717/peerj.8113
540

541 **Iliev MN, Hadjiev VG, Litvinchuk AP. 2013**. Raman and infrared spectra of brookite
542 (TiO_2): Experiment and theory. *Vibrational Spectroscopy*. **64**, 148-152.
543 https://doi.org/10.1016/j.vibspec.2012.08.003
544

545 **IUPAC. 1985**. Reporting physisorption data for gas/solid systems with special reference to
546 the determination of surface area and porosity. *Pure Appl. Chem*. **57**, 603-619.
547 http://dx.doi.org/10.1351/pac198557040603
548

549 **Jiang P, Ren DB, He DP, Fu WS, Wang J, Gu M. 2014.** An easily sedimentable and
550 effective TiO$_2$ photocatalyst for removal of dyes in water. *Sep. Purif. Technol*. **122**, 128-132.
551 https://doi.org/10.1016/j.seppur.2013.10.048

553 **Jiang X, Herricks T. Xia Y. 2003.** Monodispersed Spherical Colloids of Titania: Synthesis,
554 Characterization, and Crystallization. *Adv. Mater*. **15**, 1205-1209.
555 https://doi.org/10.1002/adma.200305105

557 **Kandiel TA, Feldhoff A, Robben L, Dillert R, Bahnemann DW. 2010.** Tailored Titanium
558 Dioxide Nanomaterials: Anatase Nanoparticles and Brookite Nanorods as Highly Active
559 Photocatalysts. *Chem. Mater*. **22**, 2050-2060. https://doi.org/10.1021/cm903472p

561 **Kumar SR, Suresh C, Vasudevan AK, Suja NR, Mukundan P, Warrier KGK. 1999.**
562 Phase transformation in sol–gel titania containing sílica. *Mater. Lett*. **38**, 161-166.
563 https://doi.org/10.1016/S0167-577X(98)00152-9
564 **Kuvarega AT, Krause RWM, Mamba B. 2015**. Evaluation of the simulated solar light
565 photocatalytic activity of N, Ir co-doped TiO$_2$ for organic dye removal from water. *Appl.*
566 *Surf. Sci*. **329**, 127-136. https://doi.org/10.1016/j.apsusc.2014.12.089

568 **Lin HY, Shih CY. 2016**. Efficient one-pot microwave-assisted hydrothermal synthesis of
569 M(M = Cr, Ni, Cu, Nb) and nitrogen co-doped TiO$_2$ for hydrogen production by
570 photocatalytic water splitting. *J. Mol. Catal. A. Chem*. **411**, 128-137.
571 https://doi.org/10.1016/j.molcata.2015.10.026

573 **Liu B, Liu LM, Lang XF, Wang HY, Lou XW, Aydil ES. 2014.** Doping high-surface-area
574 mesoporous TiO$_2$ microspheres with carbonate for visible light hydrogen production. *Energy.*
575 *Enviro*. Sci. **7**, 2592-2597. https://doi.org/10.1039/C4EE00472H

577 **Liu CS, Li F. 2012.** Natural path for more precise determination of band gap by optical
578 spectra. *Opt. Commun*. **285**, 2868-2873. https://doi.org/10.1016/j.optcom.2012.02.049

580 **Liu GL, Han C, Pelaez M, Zhu DW, Liao SJ, Likodimos V, Ioannidis N, Kontos AG,**
581 **Falaras P, Dunlop PSM. 2012**. Synthesis, characterization and photocatalytic evaluation of
582 visible light activated C-doped TiO$_2$ nanoparticles. *Nanotechnology*. **23**, 294003.
583 https://doi.org/10.1088/0957-4484/23/29/294003

585 **Luevano-Hipolito E, Matinez-De La Cruz A, Lopez-Cuellar E, Yu QL, Brouwers HJH.**
586 **2014**. Synthesis, characterization and photocatalytic activity of WO$_3$/TiO$_2$ for NO removal
587 under UV and visible light irradiation. *Mater. Chem. Phys*. **148**, 208-213.
588 https://doi.org/10.1016/j.matchemphys.2014.07.034

590 **Machado AEH, Santos LMS, Borges KA, Batista PS, Paiva VAB, Muller PS, Oliveira**
591 **DF, França MD. 2012**. Potential Applications for Solar Photocatalysis: From Environmental
592 Remediation to Energy Conversion. *Solar Radiation*. **19**, 339-378.
593 https://doi.org/10.5772/34849

595 **Machado AEH, Franca MD, Velani V, Magnino GA, Velani HMM, Freitas FS, Muller
596 PS, Sattler C, Schmucker M. 2008.** Characterization and Evaluation of the Efficiency of
597 TiO_2/Zinc Phthalocyanine Nanocomposites as Photocatalysts for Wastewater Treatment
598 Using Solar Irradiation. *Int. J. Photoenergy.* Article ID 482373.
599 https://doi.org/10.1155/2008/482373
600
601 **Machado AEH, Miranda JA, Freitas RF, Duarte ETFM, Ferreira LF, Albuquerque
602 YDT, Ruggiero R, Sattler C, Oliveira LJ. 2003**. Destruction of the organic matter present
603 in effluent from a cellulose and paper industry using photocatalysis. *Photochem. Photobiol.,
604 A.* **155**, 231-241. https://doi.org/10.1016/S1010-6030(02)00393-3
605
606 **Machado WA, Alves HO, Machado AEH. 2019**. Synthesis and Evaluation of the
607 Photocatalytic Activity of Nanostructured Composites Based on SiO_2 Recovered by TiO_2.
608 *Orbital: Electron. J. Chem*. **11**, 83-90. http://dx.doi.org/10.17807/orbital.v11i2.1347
609
610 **Martin-Somer M, Benz D, Ommen JRV, Marugan J. 2020**. Multitarget Evaluation of the
611 Photocatalytic Activity of P25-SiO_2 Prepared by Atomic Layer Deposition. *Catalysts*, **10**,
612 450-163. https://doi.org/10.3390/catal10040450
613
614 **Mohammadi S, Harvey A, Boodhoo KVK. 2014.** Synthesis of TiO_2 nanoparticles in a
615 spinning disc reactor. *Chem. Eng. J.* **258**, 171-184. https://doi.org/10.1016/j.cej.2014.07.042
616
617 **Myilsamy M, Murugesan V, Mahalakshmi M. 2015.** The Effect of Synthesis Conditions
618 on Mesoporous Structure and the Photocatalytic Activity of TiO_2 Nanoparticles. *J. Nanosci.
619 Nanotechnol*. **15**, 4664-4675. https://doi.org/10.1166/jnn.2015.9772
620
621 **Nakhjavani SH, Tavakoli O, Akhlaghi SP, Salehi Z, Esmailnejad-Ahranjani P,
622 Arpanaei A. 2015**. Efficient photocatalytic degradation of organic pollutants by
623 magnetically recoverable nitrogen-doped TiO_2 nanocomposite photocatalysts under visible
624 light irradiation. *Environ. Sci. Pollut. Res. Int.* **22**, 18859-18873.
625 https://doi.org/10.1007/s11356-015-5032-3
626
627 **Neto JOM, Bellato CR, Souza CHF, Silva RC, Rocha PA. 2017.** Synthesis,
628 Characterization and Enhanced Photocatalytic Activity of Iron Oxide/Carbon Nanotube/Ag-
629 doped TiO2 Nanocomposites. *J. Braz. Chem.* **28***, 2301-2312*.
630 http://dx.doi.org/10.21577/0103-5053.20170081
631
632 **Oancea P, Meltzer V. 2014**. Kinetics of tartrazine photodegradation by UV/H_2O_2 in aqueous
633 solution. *Chem. Pap*. **68**, 105-111. https://doi.org/10.2478/s11696-013-0426-5
634
635 **Oliveira DFM, Batista PS, Müller Jr PS, Velani V, França MD, Souza DR, Machado
636 AEH. 2012.** Evaluating the effectiveness of photocatalysts based on titanium dioxide in the
637 degradation of the dye Ponceau 4R. *Dyes Pigm*. **92**, 563-572.
638 https://doi.org/10.1016/j.dyepig.2011.06.007
639

640 **Patrocinio AOT, Scheider J, França MD, Santos LM, Caixeta BP, Machado AEH,**
641 **Bahnemann DW. 2015**. Charge carrier dynamics and photocatalytic behavior of TiO_2
642 nanopowders submitted to hydrothermal or conventional heat treatment. *RSC Adv*. **5**, 70536-
643 70545. https://doi.org/10.1039/C5RA13291F
644
645 **Patterson EM, Shelden CE, Stockton BH. 1977**. Kubelka-Munk optical properties of a
646 barium sulfate white reflectance standard. *Appl. Opt*. **16**, 729-732.
647 https://doi.org/10.1364/AO.16.000729
648
649 **Resende SF, Gouveia RL, Oliveira BS, Vasconcelos WL, Augusti R. 2017**. Synthesis of
650 $TiO_2/SiO_2-B_2O_3$ Ternary Nanocomposites: Influence of Interfacial Properties on their
651 Photocatalytic Activities with High Resolution Mass Spectrometry Monitoring *J. Braz.*
652 *Chem*. **28**, 1995-2003. http://dx.doi.org/10.21577/0103-5053.20170044
653
654 **Roisnel T, Rodriguez-Carvajal J. 2001**. WinPLOTR: a Windows tool for powder
655 diffraction patterns analysis *Mater. Sci. Forum*. **378**, 118-123.
656 https://doi.org/10.4028/www.scientific.net/MSF.378-381.118
657
658 **Rusinque B, Escobedo S, Lasa H. 2020**. Photoreduction of a Pd-Doped Mesoporous TiO_2
659 Photocatalyst for Hydrogen Produciton under Visible Light. *Catalysts*, **10**, 74-98.
660 https://doi.org/10.3390/catal10010074
661
662 **Sahoo S, Arora AK, Sridharan V. 2009.** Raman Line Shapes of Optical Phonons of
663 Different Symmetries in Anatase TiO_2 Nanocrystals. *J. Phys. Chem. C*. **113**, 16927-16933.
664 https://doi.org/10.1021/jp9046193
665
666 **Santos LM, Amorim KP, Andrade LS, Batista PS, Trovó AG, Machado AEH. 2015b**.
667 Dye Degradation Enhanced by Coupling Electrochemical Process and Heterogeneous
668 Photocatalysis. *J. Braz. Chem. Soc*. **26**, 1817-1823. https://doi.org/10.5935/0103-
669 5053.20150158
670
671 **Santos LM, Machado WA, França MD, Borges KA, Paniago RM, Patrocínio AOT,**
672 **Machado AEH. 2015a.** Structural characterization of Ag-doped TiO_2 with enhanced
673 photocatalytic activity. *RSC Adv*. **5**, 103752-103759. https://doi.org/10.1039/C5RA22647C
674
675 **Selcuk MZ, Boroglu MS, Boz I. 2012**. Hydrogen production by photocatalytic water
676 splitting using nitrogen and metal co-doped TiO_2 powder photocatalyst. *Reac. Kinet. Mech.*
677 *Cat*. **106**, 313-324. https://doi.org/10.1007/s11144-012-0434-4
678
679 **Tay Q, Liu X, Tang Y, Jiang Z, Sum TC, Chen Z. 2013**. Enhanced Photocatalytic
680 Hydrogen Production with Synergistic Two-Phase Anatase/Brookite TiO_2 Nanostructures. *J.*
681 *Phys. Chem. C*. **117**, 14973-14982. https://doi.org/10.1021/jp4040979
682
683 **Tractz GT, Viomar A, Dias BV, Lima CA, Banczec EP, Cunha MT, Antunes SRM,**
684 **Rodrigues PRP. 2019**. Recombination Study of Dye Sensitized Solar Cells with Natural
685 Extracts. *J. Braz. Chem*. **30**, 371-378. http://dx.doi.org/10.21577/0103-5053.20180186

686

687   **Wang Y. 2000**. Solar photocatalytic degradation of eight commercial dyes in TiO_2
688   suspension. *Water Res.* **34**, 990-994. https://doi.org/10.1016/S0043-1354(99)00210-9
689

690   **Yuan YJ, Tu JR, Ye ZJ, Lu HW, Ji ZG, Hu B, Li YH, Cao DP, Yu ZT, Zou ZG. 2015.**
691   Visible-light-driven hydrogen production from water in a noble-metal-free system catalyzed
692   by zinc porphyrin sensitized MoS_2/ZnO. *Dyes and Pigments*. **123**, 285-292.
693   https://doi.org/10.1016/j.dyepig.2015.08.014
694

695   **Zhang X, Yu L, Zhuang C, Peng T, Li R, Li X. 2013**. Highly efficient visible/near-IR-
696   light-driven photocatalytic H_2 production over asymmetric phthalocyanine-sensitized TiO_2.
697   *RSC Adv.* **3**, 14363-14370. https://doi.org/10.1039/C3RA41975D
698

699   **Zhu WD, Wang CW, Chen JB, Li DS, Zhou F, Zhang HL. 2012**. Enhanced field emission
700   from hydrogenated TiO_2 nanotube arrays. *Nanotechnology*. **23**, 455204.
701   https://doi.org/10.1088/0957-4484/23/45/455204

Peerⅉ Chemistry Journals
Analytical, Inorganic, Organic, Physical, Materials Science

Figure 1

Assembly used in hydrogen production assays

Image of the assembly used in hydrogen production assays: a) external view, b) internal view.
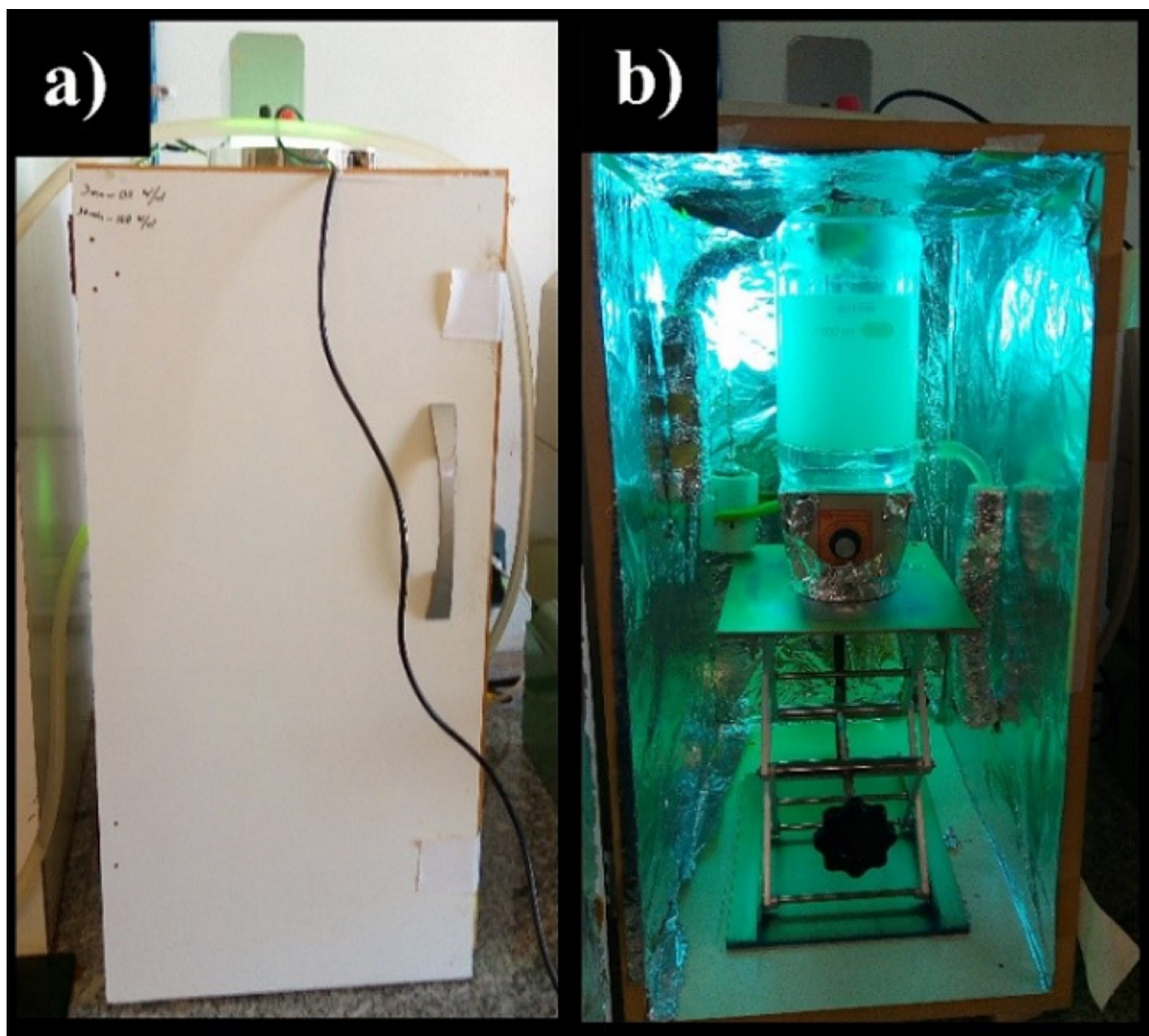
Figure 2

Ray diffratogram of the studied oxides.

Ray diffratogram of the studied oxides.
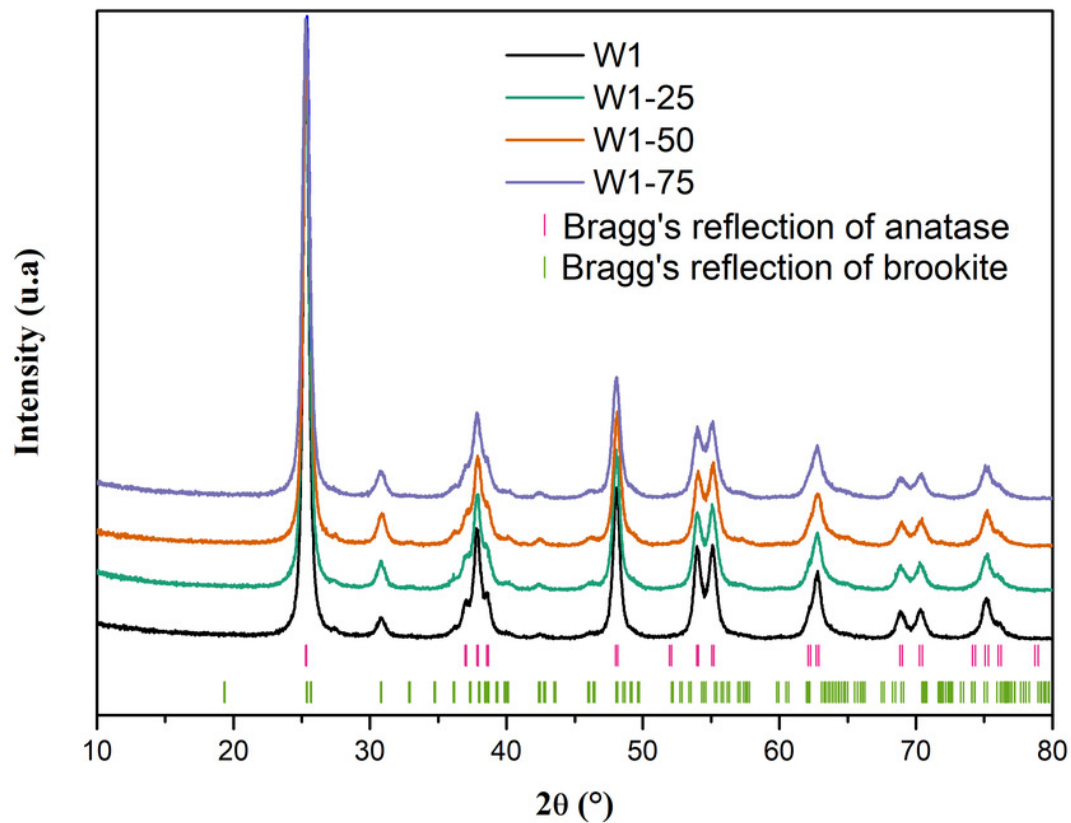
Figure 3

Raman spectra of the synthesized photocatalysts. Insert peaks at 247 cm^{-1}, 323 cm^{-1}, 368 cm^{-1}, and 456 cm^{-1} attributed to brookite.

Raman spectra of the synthesized photocatalysts. Insert peaks at 247 cm^{-1}, 323 cm^{-1}, 368 cm^{-1}, and 456 cm^{-1} attributed to brookite.
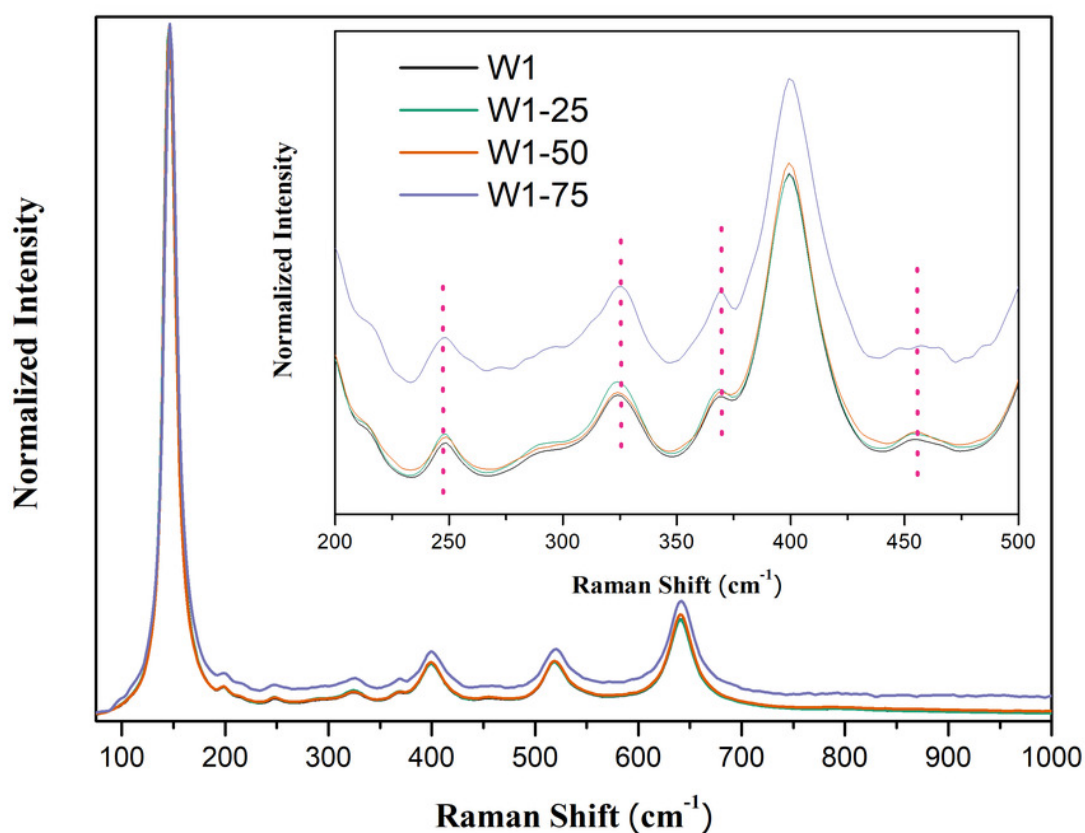
Figure 4

Expanded Raman spectra in the region between 120 and 180 cm^{-1} for the synthesized photocatalysts.

Expanded Raman spectra in the region between 120 and 180 cm^{-1} for the synthesized photocatalysts.
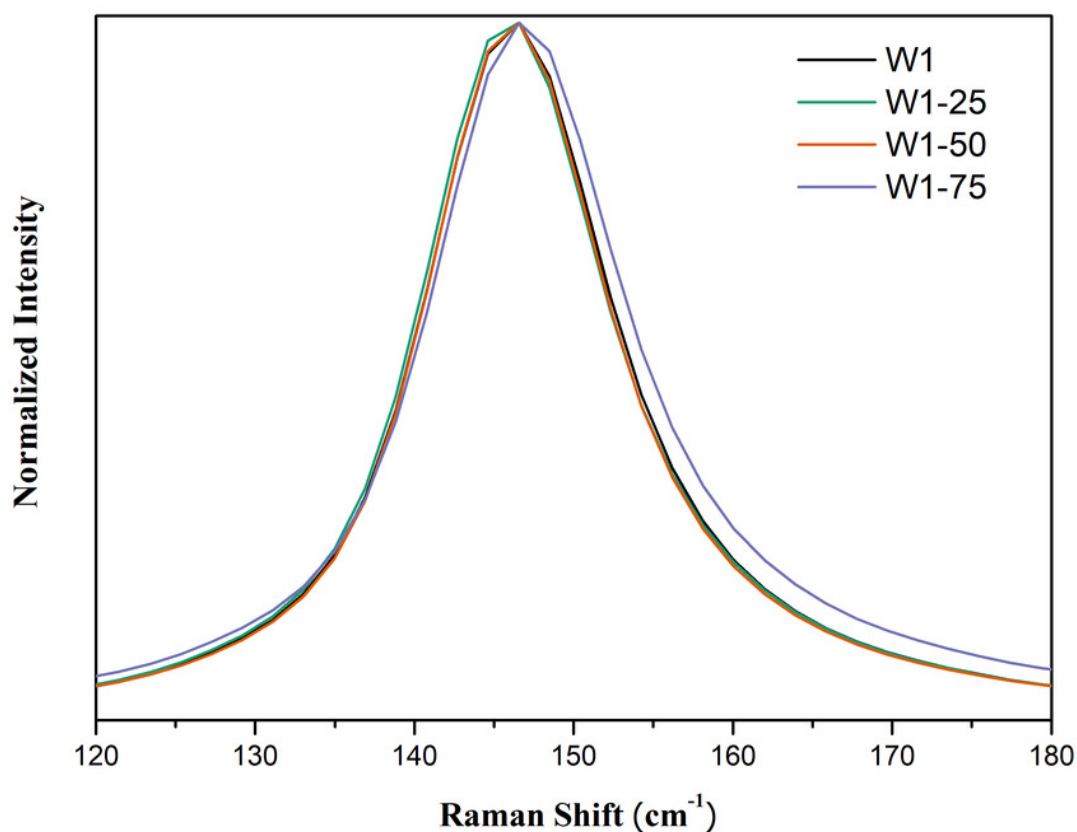
Figure 5

Diffuse reflectance spectra expressed in terms of Kubelka-Munk's function. Insert: %Reflectance vs wavelength (nm) spectra for the synthesized photocatalysts.

Diffuse reflectance spectra expressed in terms of Kubelka-Munk's function. Insert:

%Reflectance vs wavelength (nm) spectra for the synthesized photocatalysts.
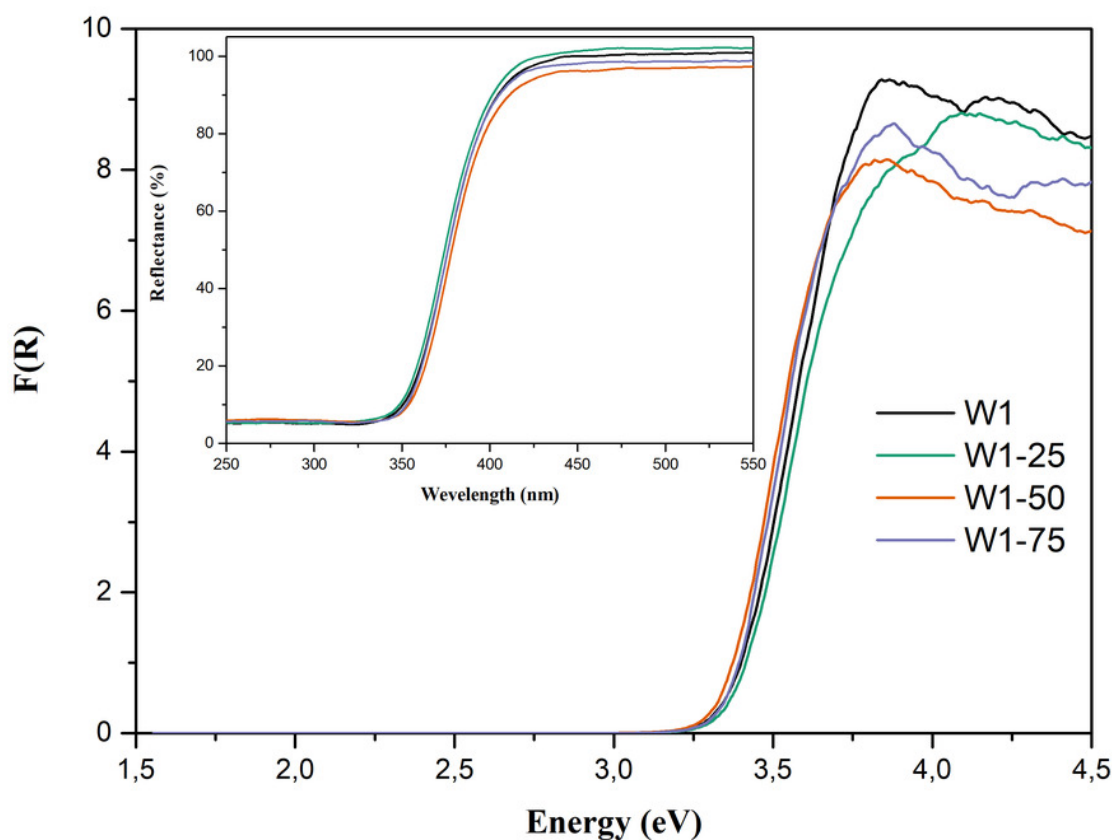
Figure 6

N$_2$ adsorption-desorption isotherms obtained for the studied photocatalysts.

N$_2$ adsorption-desorption isotherms obtained for the studied photocatalysts.
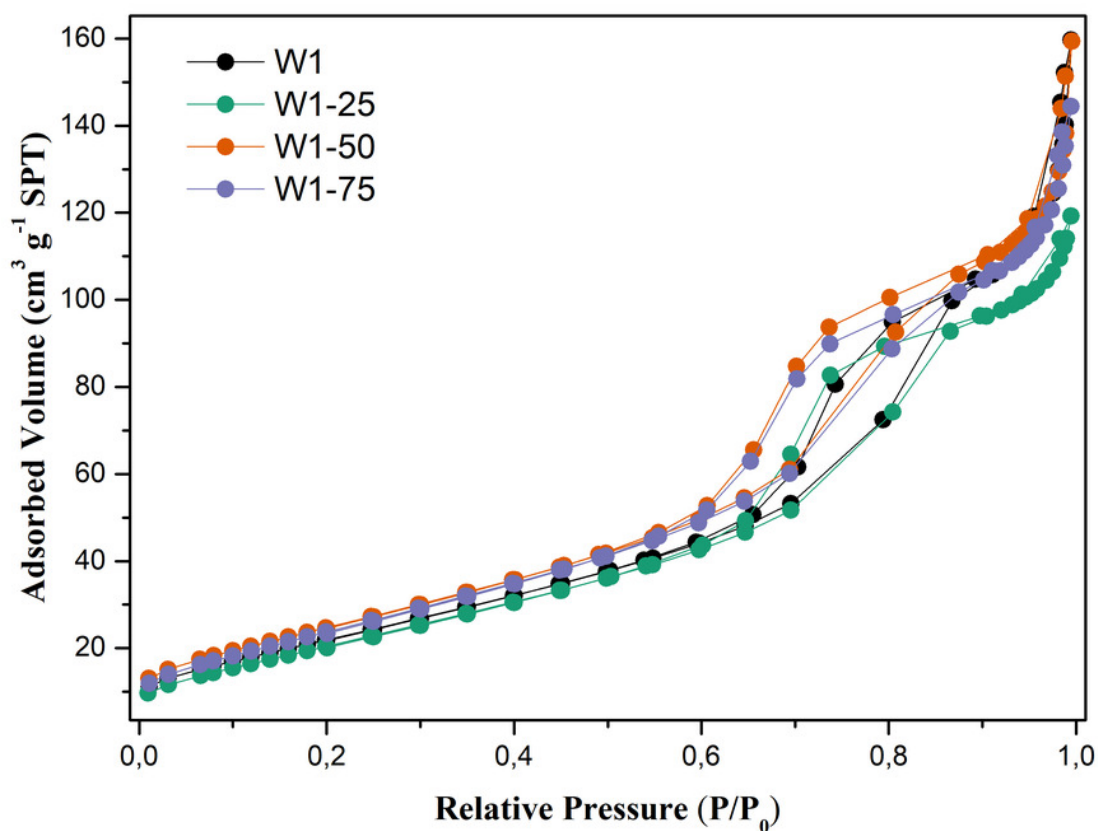
Figure 7

Images obtained by TEM for synthesized oxides a) W1, b) W1-25, c) W1-50, d) W1-75.

Figure 7 - Images obtained by TEM for synthesized oxides a) W1, b) W1-25, c) W1-50, d) W1-75.
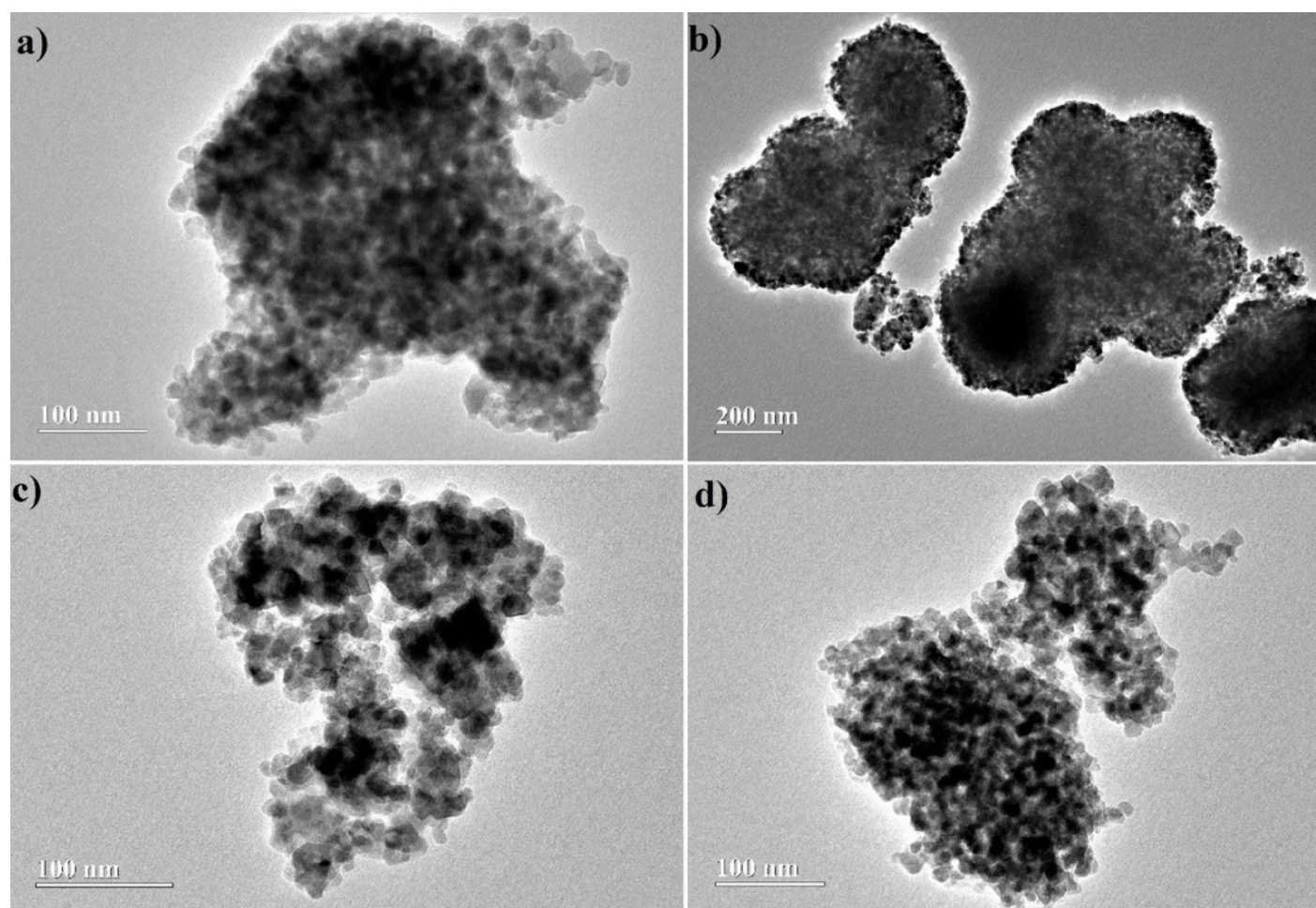
Figure 8

Photocatalytic hydrogen production vs Reaction time.

Photocatalytic hydrogen production vs Reaction time.
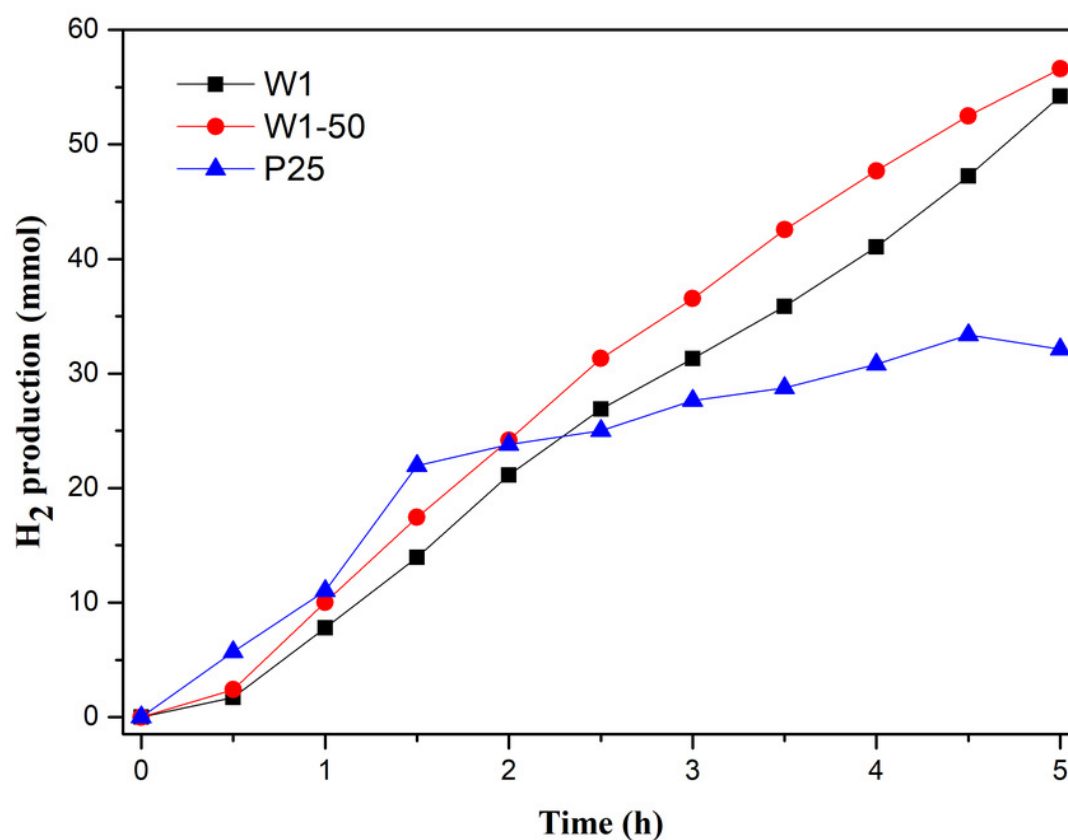
Figure 9

Amount of H$_2$ produced by W1-50 in three photocatalytic cycles.

Amount of H$_2$ produced by W1-50 in three photocatalytic cycles.

Chemistry Journals
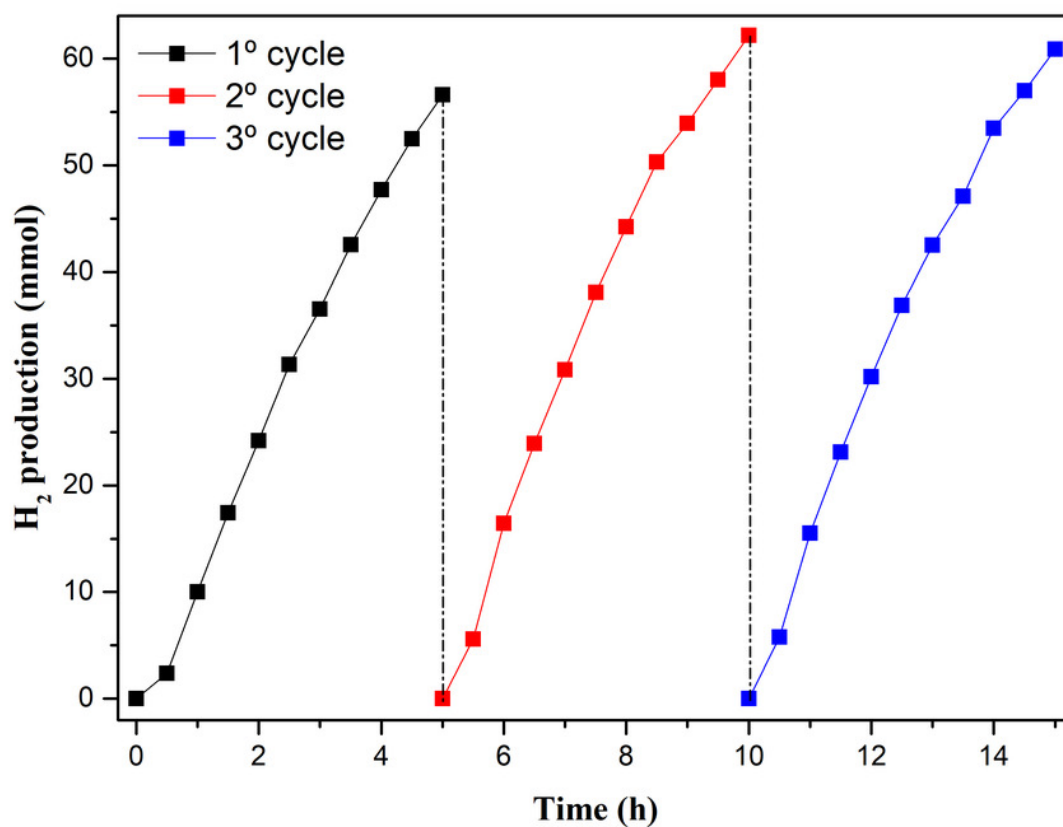
Analytical, Inorganic, Organic, Physical, Materials Science

Percentage of crystalline phase, crystallite size and medium deformation, obtained by Rietveld refinement for the synthesized oxides.

Percentage of crystalline phase, crystallite size and medium deformation, obtained by Rietveld refinement for the synthesized oxides.

2 **Table 1.** Percentage of crystalline phase, crystallite size and medium deformation, obtained by

3 Rietveld refinement for the synthesized oxides.

Oxide	Crystalline phase (%)		Crystallite medium size (nm)	Crystallite medium deformation (%)
W1	Anatase	87	61	4.0
	Brookite	13	16	8.0
W1-25	Anatase	78	64	6.0
	Brookite	22	10	6.0
W1-50	Anatase	78	63	6.0
	Brookite	22	14	10
W1-75	Anatase	78	44	5.0
	Brookite	22	22	11

Morphological parameters related to the synthesized photocatalysts.

2 **Table 1.** Morphological parameters related to the synthesized photocatalysts.

3 Photocatalyst	Surface area (m^2/g)	Porosity (%)	Mean pore diameter (nm)	Average particle size (nm)
W1	84 ± 2	21	8	14 ± 1
W1-25	80 ± 2	17	7	17 ± 3
W1-50	94 ± 2	21	7	10 ± 1
W1-75	92 ± 2	20	7	13 ± 1

 Chemistry Journals
Analytical, Inorganic, Organic, Physical, Materials Science

Photocatalytic performance of the synthesized oxides and TiO2-P25 compared with direct photolysis, in the degradation of the dyes Ponceau 4R (P4R) and Remazol Red 120 (RR120).

2 **Table 1.** Photocatalytic performance of the synthesized oxides and TiO2-P25 compared with direct

3 photolysis, in the degradation of the dyes Ponceau 4R (P4R) and Remazol Red 120 (RR120).

Dye/Reaction	Direct photolysis	W1	W1-25	W1-50	W1-75	P25
P4R						
Mineralization (%)	13±1	70±3	74±3	83±3	87±3	94±3
1st k_{min} (x10^3 min^{-1})	0.8	5.0	5.5	6.0	8.0	10
R^2	0.977	0.982	0.967	0.973	0.992	0.982
2nd k_{min} (x10^3 min^{-1})	-	12	14	21	23	33
R^2	-	0.979	0.981	0.990	0.998	0.974
Discoloration (%)	30±1	100	100	100	100	100
1st k_{disc} (x10^3 min^{-1})	2.0	25	31	30	31	51
R^2	0.989	0.999	0,998	0.999	0.998	0.997
2nd k_{disc} (x10^3 min^{-1})	-	43	73	73	97	-
R^2	-	0.972	0.937	0.932	0.876	-
RR120						
Mineralization (%)	17±2	78±2	**	79±2	**	81±1
1st k_{min} (x10^3 min^{-1})	1.4	9.0	**	8.5	**	5.6
R^2	0.959	0.995	**	0.997	**	0.992
2nd k_{min} (x10^3 min^{-1})	*	13	**	14	**	20
R^2	-	0.989	**	0.961	**	0.993
Discoloration (%)	21±1	100	**	100	**	100
1st k_{disc} (x10^3 min^{-1})	1.5	40	**	44	**	52
R^2	0.979	0.979	**	0.977	**	0.997
2nd k_{disc} (x10^3 min^{-1})	*	*	**	*	**	*
R^2	-	-	**	-	**	-

4   *Not observed; **Not determined for this catalyst